

# Schwarz–Christoffel methods for conformal mapping of regions with a periodic boundary

J.M. Floryan \*

*Department of Mechanical Engineering, Faculty of Engineering Science, The University of Western Ontario, London, Ont., Canada*

Charles Zemach

*Theoretical Division, Los Alamos National Laboratory, Los Alamos, NM, United States*

Received 28 February 1992

Revised 23 June 1992

## *Abstract*

Floryan, J.M. and C. Zemach, Schwarz–Christoffel methods for conformal mapping of regions with a periodic boundary, *Journal of Computational and Applied Mathematics* 46 (1993) 77–102.

Numerical conformal mapping methods for regions with a periodic boundary have been developed. These methods are based on the generalized Schwarz–Christoffel equation and can deal with boundary curves of arbitrary forms, i.e., made up of one or more rectifiable Jordan curves. High-order quadrature rules have been implemented in order to increase accuracy of the mapping. This is of particular relevance to highly accurate grid generation techniques required by, for example, implementation of high-order compact finite-difference discretization schemes.

**Keywords:** Conformal mapping; Schwarz–Christoffel equation; numerical grid generation.

## 1. Introduction

Let  $z = z(w)$  denote a one-to-one conformal map from a standard region  $R_w$  of the “computational” plane  $w = u + iv$  to a region  $R_z$  of irregular boundary in the “physical plane”  $z = x + iy$ . We have shown [3] how equations of the Schwarz–Christoffel type describing conformal transformations can be constructed explicitly in rather general circumstances, namely whenever Green’s function for the standard region, satisfying constant normal deriva-

*Correspondence to:* Prof. J.M. Floryan, Department of Mechanical Engineering, Faculty of Engineering Science, The University of Western Ontario, London, Ontario, Canada N6A 5B9.

\* This author’s research was supported by the NSERC of Canada grant.

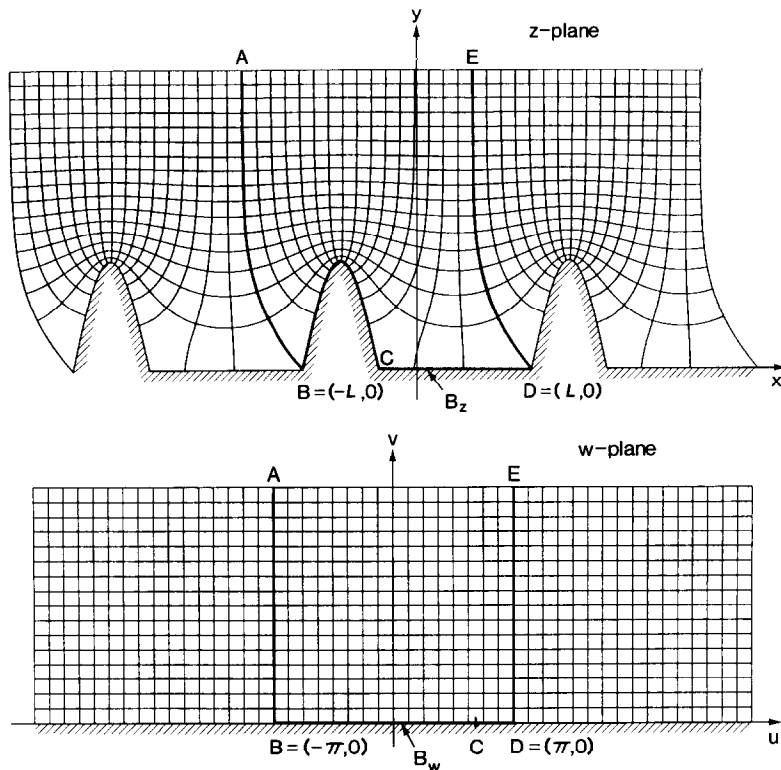


Fig. 1. Mapping between a straight and an arbitrary but periodic wall.

tive boundary conditions, can be constructed explicitly. As an application, we now explore how the relevant Schwarz–Christoffel equation (SCE) can be used for numerical conformal mapping between a half-plane and a semi-infinite two-dimensional region with a periodic, but otherwise irregular boundary, i.e., a “periodical wall” (see Fig. 1).

These numerical procedures are relevant to grid generation for the study of fluid flows in 2D regions bounded by a periodic wall, and to potential flow problems in such regions, which may be simplified by reference to some standard region with regular boundaries for purposes of computation. Applications to heat conduction, mass diffusion, electrostatics, etc., can also be identified. The periodic boundary may be polygonal, smooth with continuously turning tangents, or piecewise smooth with corners.

The mapping for regions bounded by periodic walls was formulated and calculated in [6,7] in terms of a logarithmic integral equation that connected the real and imaginary parts of  $z(w)$  on the boundary. The numerical procedure utilized interspersed Gaussian quadrature for approximating the integrals and a Newton–Raphson technique for solving the resulting nonlinear algebraic equations. High accuracy was possible even in cases of severe crowding.

Floryan [2] applied the Schwarz–Christoffel formulation for a nonperiodic boundary to the periodic problem, employing successively more periods to converge to the periodic result. This exploited two ideas earlier used in [1,8], namely, a scaling method for iteration of an initial

estimate for the boundary data, and a modified midpoint quadrature rule for the relevant singular integrals. The method was found to be too expensive in terms of computer resources, at least for some practical applications, because many periods were needed for acceptable accuracy levels.

Hoekstra [5] has applied the SCE and the Davis technique to mapping to a unit disc.

The main purposes of this paper are the following.

(1) *Improvement of Floryan's method* by exploiting the generalized SCE, as obtained in [3]. This takes periodicity into account directly.

(2) *Improvement of integration accuracy* by use of higher-order quadrature rules. Davis [1] suggested that the leading term in the error in his integration rule was of order  $\Delta^2$ , where  $\Delta$  is the length of the subintervals into which the interval of integration was divided. We have shown [4] that this is not generally the case. If a region boundary has a corner with an interior angle  $\phi$ , integrals with singularities of type  $x^\alpha$ ,  $\alpha = -1 + \phi/\pi$ , will be met. Then Davis' rule will have errors of order  $\Delta^{2+\alpha}$ ,  $\Delta^2$  and  $\Delta^2 \log(1/\Delta)$ . A sharp corner, i.e., one with  $\alpha$  close to  $-1$ , could lead to errors larger than Davis anticipated. In [4], we also developed a series of modified Newton-Cotes rules of higher order. As shown in Section 4, appropriate use of a modified Simpson's rule or modified four-point rule can reduce the order of error to  $\Delta^4$  and  $\Delta^4 \log(1/\Delta)$ . Equivalent higher-order rules for regions bounded by smooth curves are developed in Section 6.

(3) *Improvement in rate of convergence* of the iteration procedure. First, the Davis-scaling process can be accelerated by an extrapolation based on the trend of convergence. This can be particularly helpful in "difficult" cases where convergence is slow. Second, a sum rule can be invoked to reduce the number of unknown data by one. Both these devices are useful primarily when the number of unknowns is small, as in mapping of a region with a polygonal boundary with a small number of sides in a basic period, e.g., five or less. The sum rule yields the map parameters exactly for the case of a saw-tooth boundary (two straight segments in a basic period, meeting at arbitrary angles) with no iterations.

(4) *Assessment of the practical limits* of the SCE methods, for extremes of boundary irregularity.

Any numerical mapping scheme will do well when  $B_z$ , the boundary of  $R_z$ , is a small perturbation of  $B_w$ , the boundary of  $R_w$ , and will do poorly if  $B_z$  is too irregular. Thus, an important figure of merit for any scheme is the degree of boundary irregularity it can handle at various levels of computational effort. Without some systematic study of this question, one cannot judge whether statements such as "the method converges to good accuracy in ten iterations", which appear in some reports, reflect the power of the method or the mildness of the examples considered.

The notion of crowding, as defined and analyzed in [6], seems to provide a good single measure of boundary irregularity. This refers to the compression of a segment of arc of  $B_z$  when mapped to the corresponding segment of  $B_w$ . We take  $|dz/dw|$  along  $B_z$  as a numerical index of crowding in segments of  $B_z$  which are continuously curved. We find  $|dz/dw| \gg 1$  at a neighbourhood of  $B_z$  with large curvature and a center of curvature interior to  $R_z$  but close to the boundary.

For example, if the region above  $y = -5 \cos x$  is mapped to a half-plane, maximum crowding is at  $(x, y) = (\pm 2n\pi, -5)$  where  $|dz/dw| = 8.6 \cdot 10^4$ . The methods of [6] handle crowding of up to  $|dz/dw| \approx 10^{10}$  without difficulty and up to  $10^{100}$  with moderate difficulty.

Limits on our SCE approach due to other aspects of crowding are discussed in Sections 4 and 6. See [10] for elementary ways to estimate crowding prior to a full map calculation.

The above characterization of crowding needs qualification for boundaries with corners, and for physical applications, if the objective is to have an indicator of the mathematical difficulty of solving a problem. At a corner interior angle less than  $\pi$ ,  $|dz/dw| = \infty$ , but the special virtue of SCE methodologies is that corner singularities are handled exactly. Now suppose that a boundary is represented by a discrete set of grid points with separations  $\Delta s$ . In non-SCE methods, one is effectively calculating a map from a smoothed boundary through the grid points. The computed  $|dz/dw|$  will be finite everywhere, and hence in gross error in a neighbourhood of the corner. The diameter of the neighbourhood of gross error would be of the order of  $\Delta s$ .

Perhaps a suitable crowding measure, as an index of difficulty when SCE methods are applied to corner problems, can be obtained by forming a smooth function  $\bar{z}(w)$  as the ratio of  $z(w)$  to the factor  $\prod_i (w - w_i)^{\alpha_i}$  which specifies the corner singularities, and taking  $|d\bar{z}/dw|$  as that measure. This puts the criteria for smooth and cornered boundaries on a consistent basis, but may be a bit tedious in application. For our study of steps with straight sides in Section 5, we take  $|\Delta z/\Delta w|$  as the measure, where  $\Delta z$  is the separation between corner points, and this seems quite adequate to represent the underlying idea.

When conformal mapping is applied to a physical problem, there will be some characteristic minimal length scale  $L$  for the physical fields. As an example,  $L$  could be the smallest wave-length of importance in an oscillatory system. Then the mapping method should deliver values of  $|\Delta z/\Delta w|$  which are accurate for  $|\Delta z| \geq L$ . If  $L$  is larger than the diameter of some interval of irregularity along a boundary, a method which treats crowding poorly in the region of irregularity may still be adequate for the practical problem.

In general, any implementation of our method, with a particular quadrature rule, becomes inaccurate in a neighbourhood of crowding, if the crowding is made sufficiently severe. The inaccuracy can be reduced by attention to avoidance of cancellation errors, choosing a higher-order quadrature rule, and use of double precision in the numerics. When all else fails, one can make separate order-of-magnitude estimates of the map function in each region of severe crowding as in [10] and patch them to calculate results which are accurate in the less-crowded regions.

Although the numerical work of this paper relates to periodic wall boundaries, the concepts and appraisals listed above have a general character and apply to SCE methods for conformal mapping in other geometries.

## 2. Formulation

### 2.1. Mapping of a region with a periodic boundary

Consider a half-infinite region of the “physical plane”  $z = x + iy$ , bounded by a piecewise smooth curve  $y = \hat{y}(x)$ , with period  $2L$ ;  $\hat{y}(x + 2L) = \hat{y}(x)$ . More generally, one might represent the boundary parametrically:  $x = \hat{x}(t)$ ,  $y = \hat{y}(t)$ ,  $-\infty < t < \infty$ ,  $\hat{x}(t + 2L) = \hat{x}(t) + 2L$ ,  $\hat{y}(t + 2L) = \hat{y}(t)$ .

We seek a conformal map  $z = z(w)$  from the upper half of the “computational plane”

$w = u + iv$  to this region. For standardization, we take the boundary points  $(x, y) = (-L, \hat{y}(-L)), (L, \hat{y}(L))$  as images of  $(u, v) = (-\pi, 0), (\pi, 0)$ , respectively, and let the points at  $\infty$  in the  $z$ - and  $w$ -planes correspond, as shown in Fig. 1. Then the freedom to assign image points allowed by the Riemann mapping theorem is fully utilized, and  $z(w)$  is uniquely determined. Both  $z$  and  $\log(dz/dw)$  are analytic functions of  $w$  in the upper-half  $w$ -plane, and the periodicity requirement on  $z$  is

$$z(w + 2\pi) = 2L + z(w).$$

Therefore,  $z(w)$  is a function of the form

$$z(w) = \frac{L}{\pi}w + iF(e^{iw}), \quad (2.1)$$

where  $F(e^{iw})$  is analytic in  $e^{iw}$  for  $|e^{iw}| < 1$ , i.e., for  $v > 0$ , and possesses a convergent series expansion for  $v > 0$ , in powers of  $e^{iw}$ . It follows that for  $v \rightarrow \infty$ ,

$$\log \frac{dz}{dw} = \log \frac{L}{\pi} + O(e^{-v}). \quad (2.2)$$

Hereafter, we consider  $w$  restricted to the periodic strip  $R_w$  characterized as

$$R_w: -\pi \leq u \leq \pi, 0 \leq v < \infty,$$

with  $(-\pi, v)$  and  $(\pi, v)$  identified as the same point.  $R_z$  is the image of  $R_w$  in the physical plane. Their lower boundaries are

$$B_w: -\pi \leq u \leq \pi, v = 0, \quad \text{and} \quad B_z: -L \leq x \leq L, y = \hat{y}(x).$$

Further notations: the real and imaginary parts of  $z(w)$  are  $x = x(u, v)$  and  $y = y(u, v)$ , and on the lower boundary, these reduce to  $x = x(u)$ ,  $y = y(u)$ . Let  $s = s(u)$  denote arc-length along  $B_z$  measured from  $s = 0$  at  $x = -L$ . Let  $\theta = \theta(u) = \theta[s]$  be the direction angle of the tangent to a point on  $B_z$ . For  $w = u$  on  $B_w$ ,

$$\log \frac{dz}{dw} = \log \left| \frac{dz}{dw} \right| + i\theta(u) = \log \frac{ds}{du} + i\theta(u). \quad (2.3)$$

Note, also, the following sum rules:

$$\int_{u=-\pi}^{\pi} d\theta(u) = 0, \quad (2.4a)$$

$$\int_{-\pi}^{\pi} \theta(u) du = 0, \quad (2.4b)$$

$$\int_{-\pi}^{\pi} u d\theta(u) = 2\pi\theta(\pi) = 2\pi\theta(-\pi). \quad (2.4c)$$

Equation (2.4a) reflects the periodicity of  $\theta(u)$ . To verify (2.4b), equate the contour integral of  $\log(dz/dw)$  around  $R_w$  to zero and take the imaginary part, noting the cancellation of the contributions from the sides and top of  $R_w$ . Equation (2.4c) follows from (2.4b) by integration by parts.

## 2.2. The generalized Schwarz–Christoffel equation

The unsubtracted form of the generalized SCE for mapping in periodic geometry [3] is

$$\frac{dz}{dw} = e^c \exp \left\{ -\frac{1}{\pi} \int_{u'=-\pi}^{\pi} \log \sin \frac{1}{2}(w-u') d\theta(u') \right\}, \quad (2.5)$$

with

$$c = \log \frac{L}{\pi} + i\theta(\pi). \quad (2.6)$$

To verify (2.6), take the limit  $v \rightarrow \infty$  in (2.5), and apply (2.2), (2.4a) and (2.4c).

The branch of the logarithm to be taken in (2.5) for  $w$  in  $R_w$  and on  $B_w$  may be consistently defined as follows. First, for  $w=u=\text{real}$ , and  $-\pi < u' < u < \pi$ ,  $\sin \frac{1}{2}(w-u')$  is real, positive, and the logarithm is taken as real. Second, analytic continuation of  $w$  into  $R_w$  and back onto  $B_w$  with  $-\pi < u < u' < \pi$  leads to values of  $q = \sin \frac{1}{2}(w-u')$  throughout the complex  $q$ -plane, but without ever crossing the negative imaginary  $q$ -axis. Hence, we may put

$$\log \sin \frac{1}{2}(w-u') = \log |\sin \frac{1}{2}(w-u')| + i\gamma, \quad -\frac{1}{2}\pi < \gamma < \frac{3}{2}\pi. \quad (2.7)$$

In particular, for  $w=u$ , i.e., for  $w$  on the real axis,

$$\log \sin \frac{1}{2}(u-u') = \begin{cases} \log |\sin \frac{1}{2}(u-u')|, & u' < u, \\ \log |\sin \frac{1}{2}(u-u')| + i\pi, & u' > u. \end{cases} \quad (2.8)$$

As noted in [3] the argument of the logarithm in the SCE for periodic geometry is not uniquely determined. The choice made here is convenient for numerical calculation. For  $w$  on the boundary, (2.5) yields a complex boundary SCE

$$\frac{dz}{du} = e^c \exp \left\{ -\frac{1}{\pi} \int_{-\pi}^{\pi} \log \sin \frac{1}{2}(u-u') d\theta(u') \right\} \quad (2.9a)$$

and, taking absolute values, a real boundary SCE

$$\left| \frac{dz}{dw} \right| = \frac{ds}{du} = \frac{L}{\pi} \exp \left\{ -\frac{1}{\pi} \int_{-\pi}^{\pi} \log |\sin \frac{1}{2}(u-u')| d\theta(u') \right\}. \quad (2.9b)$$

Equation (2.9b) is an integro-differential equation relating  $ds/du$  and  $d\theta/du$ , to be solved in conjunction with the given boundary equation  $y = \hat{y}(x)$  which relates  $s$  to  $\theta$ . Equation (2.9a) also equates the phase of  $dz/du$  to the phase of the right-hand side. This phase relation is an identity in view of (2.3), (2.6) and (2.8). Section 3 will describe iteration methods for solving both (2.9a) and (2.9b).

To make the connection between the generalized SCE (2.5) and Floryan's earlier formulation for periodic geometry [2] we approximate the sine by a finite number of factors in its representation as an infinite product:

$$\sin \frac{1}{2}(w-u') \approx \frac{1}{2}(w-u') \prod_{k=1}^N \left[ 1 - \frac{(w-u')^2}{(2\pi k)^2} \right].$$

Then,

$$\log \sin \frac{1}{2}(w - u') \approx \sum_{k=-N}^N \log(w - u' - 2k\pi) + \text{const.}$$

Substituting this into (2.5) and noting that the constant gives zero contribution to the integral, we obtain the approximate SCE of [2]. The error in this estimate of  $\log \sin \frac{1}{2}(w - u')$  is

$$\sum_{k=N+1}^{\infty} \log \left[ 1 - \frac{(w - u')^2}{(2\pi k)^2} \right],$$

which, for large  $N$ , is approximately

$$\frac{(w - u')^2}{4\pi^2} \sum_{k=N+1}^{\infty} \frac{1}{k^2}.$$

The sum over  $k$  is of order  $1/N$ , in agreement with the error estimate of [2].

### 2.3. Treatment of corners

Let  $z_i = z(u_i)$  be a boundary point at which two arcs or straight segments of  $B_z$  meet at a corner. With  $\epsilon$  denoting a positive infinitesimal, let  $\theta(u_i + \epsilon)$ ,  $\theta(u_i - \epsilon)$  denote the tangent directions of either side of the corner. Define a turning angle  $\Delta\theta_i$  and turn parameter  $\alpha_i$  by

$$\Delta\theta_i = \theta(u_i + \epsilon) - \theta(u_i - \epsilon), \quad (2.10)$$

$$\alpha_i = -\frac{\Delta\theta_i}{\pi}. \quad (2.11)$$

In general,  $B_w$  is divided into segments, whose images in the physical plane are smooth segments of  $B_z$ , and which are separated by nodes  $u_i$  marking the corners. If  $f(u)$  is any smooth function on  $B_w$ ,

$$\frac{1}{\pi} \int_{-\pi}^{\pi} f(u') d\theta(u') = - \sum_i \alpha_i f(u_i) + \frac{1}{\pi} \sum_j \int_{u_{j-1}}^{u_j} f(u') \frac{d\theta(u')}{du'} du'. \quad (2.12)$$

The  $i$ -sum is over corners and the  $j$ -sum is over Riemann integrals on the segments. In this representation, the generalized SCE becomes

$$\frac{dz}{dw} = e^c \prod_i [\sin \frac{1}{2}(w - u_i)]^{\alpha_i} \prod_j \exp \left\{ -\frac{1}{\pi} \int_{u_{j-1}}^{u_j} \log \sin \frac{1}{2}(w - u') \frac{d\theta(u')}{du'} du' \right\}. \quad (2.13)$$

If  $B_z$  is composed of straight segments only, the  $j$ -product in (2.13) is replaced by unity (because  $d\theta/du = 0$ ). The more familiar product form of an SCE for a polygonal boundary emerges as a special case of the continuous form, rather than the other way around, as in most earlier derivations of SCEs.

For  $B_z$  composed of straight segments only, the sum rules (2.4a), (2.4b) become

$$\sum_i \alpha_i = 0, \quad (2.14a)$$

$$\sum_j \theta_j \Delta u_j = 0. \quad (2.14b)$$

Here,  $\theta_j$  is the direction in the physical plane of the  $j$ th segment and  $\Delta u_j$  is the  $u$ -interval which maps into that segment.

It may be expedient in a corner problem to place one corner at  $x = -L$ , and hence also at  $x = +L$ . Then in the computation plane, the corner is both at  $u = -\pi$  and  $u = \pi$ . To maintain clarity in the integration over jumps in  $d\theta(u')$ , one may shift the  $u'$ -integration to the interval  $(-\pi + \epsilon, \pi + \epsilon)$ . This amounts to a convention that the corner is considered wholly at  $u = \pi$ , and not at all at  $u = -\pi$ . In (2.6),  $\theta(\pi)$  would be interpreted as  $\theta(\pi + \epsilon)$ , i.e., the tangent direction on the right side of the corner at  $u = \pi$ .

#### 2.4. Reflection symmetry

Suppose  $B_z$  is either symmetric or anti-symmetric about  $x = 0$ . Then  $z = (0, \hat{y}(0))$  will be the image of  $w = (0, 0)$ . We will have  $\theta(-u) = -\theta(u)$  for the symmetric case and  $\theta(-u) = \theta(u)$  for the anti-symmetric case. Both cases allow the integral over  $d\theta(u)$  on  $[-\pi, 0]$  to be replaced by an integral on  $[0, \pi]$  affording a reduction in computation effort.

For symmetry about the middle of the boundary, the SCE (2.5) becomes

$$\frac{dz}{dw} = e^d \exp \left\{ -\frac{1}{\pi} \int_0^\pi \log(\cos w - \cos u') d\theta(u') \right\}, \quad (2.15)$$

with

$$d = \log \frac{2L}{\pi} + i\theta(\pi) - \frac{1}{\pi} \log(\sin \frac{1}{2}u) \Delta\theta(0) - \frac{1}{\pi} \log(\cos \frac{1}{2}u) \Delta\theta(\pi).$$

For anti-symmetry, we find

$$\frac{dz}{dw} = e^c \exp \left\{ -\frac{1}{\pi} \int_0^\pi \log \left( \frac{\sin \frac{1}{2}(u - u')}{\sin \frac{1}{2}(u + u')} \right) d\theta(u') \right\}, \quad (2.16)$$

with  $c$  given by (2.6).

### 3. Iteration and scaling

#### 3.1. Preliminaries

The first step in solving the SCE is to solve for  $z = z(u)$  on the boundaries. Choosing a suitably dense set of points  $z = \{z_k\}$ ,  $0 \leq k \leq N$  on  $B_z$ , we calculate data  $u = \{u_k\}$ , such that  $z_k = z(u_k)$ , by successive improvements of an initial estimate. The  $n$ th approximant  $u^{(n)}$  is tested in either the real or the complex boundary SCE, and discrepancies are used to define the next approximation  $u^{(n+1)}$  by simple scaling laws. Computation time per iteration for  $B_z$

composed of straight segments is proportional to the number  $N_I$  of integration intervals and to the number  $N_c$  of corners. Time per iteration for a smoothly curved boundary depends on  $N_I$  and on the number of unknowns (which equals  $N_I$ ), and so is proportional to  $(N_I)^2$ . Variation of quadrature error with  $N_I$  depends on the quadrature rule, and is illustrated in the numerical examples.

The calculation finds the mapping  $z \rightarrow u$  from the physical plane to the computational plane for a set of boundary points. Afterwards, the Schwarz–Christoffel formula delivers the inverse map  $w \rightarrow z$  for any  $w$ . Given an arbitrary  $z'$  in the physical plane, the pre-image  $w'$  would be found by an interpolation or inversion process.

The present methods of iteration and scaling are like those of [1,2,5,8], with four embellishments. First, we recognize and explain the difference between choosing the complex boundary SCE and the real boundary SCE for defining the iteration, and alternatives related to the “phase condition” (Section 3.3). Second, we show how convergence of the iteration can be accelerated, for saving of computer time in problems with significant crowding. Third, we show how the sum rule (2.14b) can be incorporated into the iteration. This reduces the number of unknown parameters by one, and, like the acceleration, is primarily useful for polygonal boundaries with a small number of the sides. Fourth and most important, we implement a variety of quadrature rules for both the inner and outer integrations.

Let  $\{z_k\}$ ,  $0 \leq k \leq N$ , be a sequence of boundary points in the physical plane, ordered in direction of increasing  $s$ , with  $z_0 = (-L, \hat{y}(-L))$ ,  $z_N = (L, \hat{y}(L))$ . Each corner must appear in the list and additional  $z_k$  can be added to improve the characterization of the curved section of  $B_z$ . The  $z_k$  may be distributed to form equal  $x$ -intervals, equal  $s$ -intervals, may be packed more densely in regions of high curvature or high crowding, etc. Define associated sequences for differences, arc lengths and tangent angles:

$$\Delta z_k = z_k - z_{k-1}, \quad 1 \leq k \leq N, \quad (3.1a)$$

$$\Delta s_k = \int_{x_{k-1}}^{x_k} \left[ 1 + \left( \frac{dy}{dx} \right)^2 \right]^{1/2} dx, \quad 1 \leq k \leq N, \quad (3.1b)$$

and  $\theta_k$ ,  $0 \leq k \leq N$ , is the direction of  $B_z$  at  $z_k$ . If  $z_k$  is a corner, there is a turn parameter  $\alpha_k$  as in (2.11), and two  $\theta_k$ 's, one for each of the adjacent segments, but no special notation will be needed. These data are presumed known from the initial specification of  $B_z$ .

Let  $\{u_k^{(0)}\}$  be an initial estimate of the  $u_k$ , with both sequences in increasing order, and

$$u_0 = u_0^{(0)} = -\pi, \quad u_N = u_N^{(0)} = \pi. \quad (3.1c)$$

Set

$$\Delta u_k^{(0)} = u_k^{(0)} - u_{k-1}^{(0)} \quad (3.1d)$$

and

$$\Delta u_k = u_k - u_{k-1}, \quad (3.1e)$$

so that

$$\sum_{k=1}^N \Delta u_k^{(0)} = \sum_{k=1}^N \Delta u_k = 2\pi \quad (3.1f)$$

and

$$\Delta u_k^{(0)} > 0, \quad \Delta u_k > 0, \quad (3.1g)$$

for all  $k$ ,  $1 \leq k \leq N$ .

Almost any choice of  $u_k^{(0)}$  is adequate for convergence of the iteration procedure. Thus, in a sloped step example of Section 5, where  $\Delta u_1 \sim 10^{-8}$  and  $\Delta u_2, \Delta u_3, \Delta u_4 \sim 1$ , the choice of equal spacing for the  $u_k^{(0)}$  did not prevent convergence, although eighteen iterations were needed to bring  $\Delta u_k^{(n)}$  down to the right order of magnitude.

### 3.2. Iteration based on the real SCE (2.9b)

Suppose the sequence  $u^{(0)}, u^{(1)}, u^{(2)}, \dots$  has been defined up to  $u^{(n)}$ . We choose (see below) an approximation  $\theta^{(n)}(u)$  to  $\theta(u)$ , and integrate (2.9b) over intervals  $\Delta u^{(n)}$  to get approximate arc lengths intervals  $\Delta s_k^{(n)}$ :

$$\Delta s_k^{(n)} = \frac{L}{\pi} \int_{u_{k-1}^{(n)}}^{u_k^{(n)}} \exp \left\{ -\frac{1}{\pi} \int_{-\pi}^{\pi} \log |\sin \frac{1}{2}(u - u')| d\theta^{(n)}(u') \right\} du. \quad (3.2a)$$

Then, separating explicitly the corner and smooth boundary contributions,

$$\Delta s_k^{(n)} = \frac{L}{\pi} \int_{u_{k-1}^{(n)}}^{u_k^{(n)}} \prod_i |\sin \frac{1}{2}(u - u_i^{(n)})|^{\alpha_i} \prod_j \exp \left\{ -\frac{1}{\pi} \text{Real}[I_j^{(n)}(u)] \right\} du, \quad (3.2b)$$

with

$$I_j^{(n)}(w) = \int_{u_{j-1}}^{u_j} \log \sin \frac{1}{2}(w - u') d\theta^{(n)}(u').$$

The  $i$ -product is over the corners and the  $j$ -product is over all the intervals  $\Delta u^{(n)}$ . The  $I_j^{(n)}$  are (complex) Riemann integrals not including any jumps in  $\theta(u)$ . If  $B_z$  is straight from  $z_{j-1}$  to  $z_j$ ,  $I_j^{(n)}(w) = 0$ .

We proceed as follows.

(a) Let  $\bar{u}_j \equiv \bar{u}_j^{(n)} = \frac{1}{2}(u_j^{(n)} + u_{j-1}^{(n)})$  be the midpoint of  $(u_{j-1}^{(n)}, u_j^{(n)})$  and let  $\Delta u_j^{(n)} = u_j^{(n)} - u_{j-1}^{(n)}$ . Let  $\theta(u')$  on  $(u_{j-1}^{(n)}, u_j^{(n)})$  be approximated by an expansion

$$\theta^{(n)}(u') = c_0 + \sum_{m=1}^M c_m \sin^{m \frac{1}{2}}(u' - \bar{u}_j). \quad (3.3)$$

This depends on  $M+1$  coefficients  $c_i$ , to be determined from data available at the  $n$ th step of iteration. It generates an  $M$ -point quadrature rule for the  $I_j^{(n)}$ :

$$I_j^{(n)}(w) = \sum_{m=1}^M c_m Q_{mj}(w), \quad (3.4)$$

where

$$Q_{mj}(w) = \int_{u'=u_{j-1}}^{u_j} \log \sin \frac{1}{2}(w - u') d(\sin^{m \frac{1}{2}}(u' - \bar{u}_j)). \quad (3.5)$$

The  $Q_{mj}$  are calculated in the Appendix. The choice of functional form in (3.3) allows analytic evaluation of (3.5).

At the minimum, the rule for  $\theta^{(n)}(u)$  should include the endpoint conditions

$$\theta^{(n)}(u_{j-1}) = \theta_{j-1}, \quad \theta^{(n)}(u_j) = \theta_j. \quad (3.6)$$

In the simplest case, only these conditions are imposed, leading to a two-point rule with

$$c_0 = \frac{1}{2}(\theta_j + \theta_{j-1}), \quad c_1 = \frac{1}{2} \frac{\theta_j - \theta_{j-1}}{\sin\left(\frac{1}{2}\Delta u_j^{(n)}\right)}, \quad I_j^n(u) = c_1 Q_{1j}(u).$$

To define a four-point rule, we can add the conditions

$$\theta^{(n)}(u_{j-2}^{(n)}) = \theta_{j-2}, \quad \theta^{(n)}(u_{j+1}^{(n)}) = \theta_{j+1}. \quad (3.7)$$

By periodicity, one can interpret  $\theta_{-1}$  and  $\theta_{N-1}$ , etc. If either  $z_j$  or  $z_{j-1}$  is a corner, one of the conditions (3.7) must be replaced by a condition at another point, or dropped.

Having chosen a rule for  $\theta^{(n)}(u')$  in each interval  $(u_{j-1}, u_j)$ , we do the “inner integration” over  $u'$  in (3.2a) for whatever  $u$ -values may be needed.

(b) Next, we choose a quadrature rule for the “outer integration” over  $u$  in (3.2b), consistent with the accuracy level of the inner integration; see Section 4. This yields a set of estimated intervals of arc lengths  $\Delta s_k^{(n)} = s_k^{(n)} - s_{k-1}^{(n)}$ . The next iterate for the  $u$ -data is then defined by  $u_0^{(n+1)} = -\pi$  and two equations

$$\Delta u_k^{(n+1)} = \frac{2\pi \Delta s_k / \Delta s_k^{(n)}}{\sum_m (\Delta u_m^{(n)} \Delta s_m / \Delta s_m^{(n)})} \Delta u_k^{(n)}, \quad (3.8a)$$

$$u_k^{(n+1)} = -\pi + \sum_{m=1}^k \Delta u_m^{(n+1)}, \quad 1 \leq k \leq N. \quad (3.8b)$$

The sum in the denominator of (3.8a) renormalizes the  $\Delta s_k / \Delta s_k^{(n)}$  scaling to maintain  $\sum_k \Delta u_k^{(n+1)} = 2\pi$ .

The iteration is continued until  $|\Delta s_k - \Delta s_k^{(n)}|$ ,  $|\Delta u_k^{(n+1)} - \Delta u_k^{(n)}|$  and  $|u_k^{(n+1)} - u_k^{(n)}|$  reach acceptably small values. Even high-precision convergence of  $u^{(n)}$  does not, however, guarantee a high-precision result, because of quadrature error. This can be tested by a series of iterations with successively smaller quadrature intervals.

### 3.3. Iteration based on the complex SCE (2.9a)

Integrating (2.9a) over  $(u_k, u_{k-1})$ , we get, in analogy to (3.2b),

$$\Delta z_k^{(n)} = z_k^{(n)} - z_{k-1}^{(n)} = e^{c \int_{u_{k-1}^{(n)}}^{u_k^{(n)}} \prod_i [\sin \frac{1}{2}(u - u_i^{(n)})]^{\alpha_i} \prod_j \exp \left\{ -\frac{I_j^{(n)}(u)}{\pi} \right\} du}. \quad (3.9)$$

The iteration follows the procedure of Section 3.2, with a revised scaling rule:

$$\Delta u_k^{(n+1)} = \frac{2\pi |\Delta z_k / \Delta z_k^{(n)}|}{\sum_m \Delta u_m^{(n)} |\Delta z_m / \Delta z_m^{(n)}|} \Delta u_k^{(n)}. \quad (3.10)$$

As  $|\Delta z_k^{(n)}|$  converges to  $|\Delta z_k|$ , the phase of  $\Delta z_k^{(n)}$  will, in general, only converge to the phase of  $\Delta z_k$  within quadrature error. This supplies a diagnostic which shows what limitation in

overall accuracy the quadrature rules are imposing. However, one may adjust the expansion (3.3) for  $\theta^{(n)}(u')$  so that the phase  $\Phi_k^{(n)}$  of  $\Delta z_k^{(n)}$  equals the phase  $\Phi_k$  of  $\Delta z_k$  for all  $k$  and  $n$ . This “phase condition” increases the accuracy of the modeling of  $\theta^{(n)}(u)$ , and decreases overall quadrature error.

We now consider two ways to implement the phase condition. Adapting (2.3) to the  $n$ th iterate, we have

$$\left(\frac{dz}{dw}\right)^{(n)} = \left(\frac{ds}{du}\right)^{(n)} e^{i\theta^{(n)}(u)},$$

provided  $z$  is not at a corner, regardless of how  $\theta^{(n)}(u)$  is modeled. Let  $\Phi_k^{(n)}$  be the phase angle of  $\Delta z_k^{(n)}$  as defined in (3.9). Then

$$\Delta z_k^{(n)} = |\Delta z_k^{(n)}| e^{i\Phi_k^{(n)}} = \int_{u_{k-1}^{(n)}}^{u_k^{(n)}} \left(\frac{dz}{dw}\right)^{(n)} du = \int_{u_{k-1}^{(n)}}^{u_k^{(n)}} \left(\frac{ds(u)}{du}\right)^{(n)} e^{i\theta^{(n)}(u)} du, \quad (3.11)$$

where the prescription for computing the  $n$ th iterate of  $ds/du$  was laid out in Section 3.2. It follows that if the quadrature for (3.11) is the midpoint rule, or the Davis rule,  $\Phi_k^{(n)} = \theta^{(n)}(\bar{u}_k)$ . The phase condition is satisfied by adding  $\theta^{(n)}(\bar{u}_k) = \Phi_k$  to the constraints determining the  $c_m$  in the expansion (3.3) of  $\theta^{(n)}(u)$ . This promotes the two-point and four-point rules for  $\theta^{(n)}(u)$  to three-point and five-point rules, respectively.

If (3.11) is evaluated by Simpson’s rule, then the condition is

$$\Phi_k = \text{phase of } \left\{ \frac{ds^{(n)}(u_{k-1}^{(n)})}{du} e^{i\theta_{k-1}} + 4 \frac{ds^{(n)}(\bar{u}_k^{(n)})}{du} e^{i\theta^{(n)}(\bar{u}_k)} + \frac{ds^{(n)}(u_k^{(n)})}{du} e^{i\theta_k} \right\},$$

or equivalently,

$$4 \frac{ds^{(n)}(\bar{u}_k)}{du} \sin(\theta^{(n)}(\bar{u}_k) - \Phi_k) = - \frac{ds^{(n)}(u_{k-1}^{(n)})}{du} \sin(\theta_{k-1} - \Phi_k) - \frac{ds^{(n)}(u_k^{(n)})}{du} \sin(\theta_k - \Phi_k). \quad (3.12)$$

Equation (3.12) determines  $\theta^{(n)}(\bar{u}_k)$  from quantities known after  $\theta^{(n)}(u)$  has been used to find them and this is awkward to implement. What we can do is regard (3.12) as an equation to determine  $\theta^{(n+1)}(\bar{u}_k^{(n+1)})$  rather than  $\alpha^{(n)}(\bar{u}_k^{(n)})$ . Thus, in the iteration step  $\mathbf{u}^{(0)} \rightarrow \mathbf{u}^{(1)}$ , we take  $\theta^{(0)}(\bar{u}_k) = \Phi_k$ , while in the later steps,  $\mathbf{u}^{(n)} \rightarrow \mathbf{u}^{(n+1)}$ , and we get  $\theta^{(n)}(\bar{u}_k^{(n)})$  from (3.12) with the  $ds/du$  data taken from the previous step. This was done in the examples of Section 6.

### 3.4. Acceleration of iteration

For  $n \geq n_0$  and  $1 \leq k \leq N-1$ , define

$$\rho_k^{(n)} = \frac{\Delta u_k^{(n)} - \Delta u_k^{(n-1)}}{\Delta u_k^{(n-1)} - \Delta u_k^{(n-2)}}. \quad (3.13)$$

Then  $\rho_k^{(n)}$  measures the rate at which approximation to  $\Delta u_k$  is being improved.

Suppose that for iterations past iteration  $n_0$ , this measure becomes essentially independent of iteration numbers. Then we can extrapolate to get an improved estimate  $\overline{\Delta u_k}$  of the true limit  $\Delta u_k$ . Define

$$a_m = \Delta u_k^{(m)} - \rho_k^{(m)} \Delta u_k^{(m-1)}.$$

For  $m \geq n_0$ , with all  $\rho_k^{(m)}$  equal to a common value  $\rho_k$ , (3.13) implies  $a_m = a_{m-1}$ . Thus,

$$(1 - \rho_k) \Delta u_k \approx \lim_{m \rightarrow \infty} a_m = a_{n_0} = \Delta u_k^{(n_0)} - \rho_k \Delta u_k^{(n_0-1)}.$$

Hence, the improved estimate is

$$\overline{\Delta u_k} = \frac{\Delta u_k^{(n_0)} - \rho_k \Delta u_k^{(n_0-1)}}{1 - \rho_k} = \frac{\Delta u_k^{(n)} \Delta u_k^{(n-2)} - (\Delta u_k^{(n-1)})^2}{\Delta u_k^{(n)} - 2 \Delta u_k^{(n-1)} + \Delta u_k^{(n-2)}}. \quad (3.14)$$

Equation (3.14) is the acceleration step to be used to define the next iterate  $\Delta u_k^{(n_0+1)}$ , rather than the normal iteration step. This procedure is, in fact, the Aitken  $\Delta^2$ -method [9].

In practice, following a possibly poor initial estimate  $\{\Delta u_k^{(0)}\}$ , a number of iterations is required to sort things out and produce an iterate  $\{\Delta u_k^{(n)}\}$  within 10–20% of true values. This number is about 3 to 5 for easy cases (low crowding), and may be longer for difficult cases.

After further iterations, the  $\rho_k^{(n)}$  do tend to a constant value due to the fact that after a succession of corrections, the effect of the largest eigenvalue of the correction matrix dominates. One may take as a criterion for constancy that the  $\rho_k^{(n)}$ , for all  $k$ , do not vary over two iterations by more than, say, 10% or 1% from a median value  $\bar{\rho}$ . When the criterion is met, the next iterate is defined by (3.14). The  $\Delta u_k^{(n+1)}$  should be rescaled so that they sum to  $2\pi$ . The acceleration may not be applied if it yields negative values of any of the  $\Delta u_k^{(n+1)}$ . This means that for  $\rho$ -values close to one, the constancy criterion should be more severe. Typically, the  $\Delta u_k^{(n+1)}$  from (3.14) are one or two orders of magnitude more accurate than the preceding  $\Delta u_k^{(n)}$ , depending on how severe a constancy criterion was met. The more severe the criterion, the larger the number of iterations required to meet it, and then to follow it before the next acceleration, so the overall acceleration of the iteration process is not, in fact, very sensitive to the criterion chosen. Examples are given in Section 5.

### 3.5. Incorporating the sum rule into the iteration

We consider only the case where  $B_z$  is made up of straight segments, so the sum rule takes the form (2.14b).

Suppose we have defined a preliminary scaling  $\Delta v_k = \Delta u_k^{(n)} |\Delta z_k / \Delta z_k^{(n)}|$  and now ask for the next iterate  $\Delta u_k^{(n+1)}$ , where each  $\Delta u_k^{(n+1)}$  is as close as possible to each  $\Delta v_k$  for all  $k$ , but the constraint  $\sum_k \Delta u_k = 2\pi$  is obeyed. The best solution seems to be the prescription already given, i.e.,

$$\Delta u_k^{(n+1)} = \frac{2\pi \Delta v_k}{\sum_k \Delta v_k}. \quad (3.15)$$

This can be inferred from a variational principle as follows. The sum

$$\sum_k \frac{1}{2\Delta v_k} (\Delta u_k - \Delta v_k)^2$$

takes on its minimum value when  $\Delta u_k = \Delta v_k$ . To determine its minimum value under the constraint  $\sum_k \Delta u_k = 2\pi$ , introduce a Lagrange multiplier  $\lambda$ , define a new sum  $S(\lambda)$ ,

$$S(\lambda) = \sum_k \frac{1}{2\Delta v_k} (\Delta u_k - \Delta v_k)^2 - \lambda \left( \sum_k \Delta u_k - 2\pi \right), \quad (3.16)$$

and require

$$\frac{\partial S(\lambda)}{\partial \Delta u_k} = 0, \quad 1 \leq k \leq n.$$

This leads directly to (3.15).

Next, we impose an additional constraint, namely the sum rule

$$\sum_k \theta_k \Delta u_k = 0.$$

Add a second Lagrange multiplier  $\mu$ , forming

$$S(\lambda, \mu) = S(\lambda) - \mu \sum_k \theta_k \Delta u_k, \quad (3.17)$$

and ask for a minimum of  $S(\lambda, \mu)$  subject to both constraints. The solution of this extended variational principle is

$$\Delta u_k = 2\pi \frac{(\sum_j \theta_j^2 \Delta v_j) \Delta v_k - (\sum_j \theta_j \Delta v_j) \theta_k \Delta v_k}{(\sum_j \theta_j^2 \Delta v_j)(\sum_j \Delta v_j) - (\sum_j \theta_j \Delta v_j)^2}. \quad (3.18)$$

This can improve convergence of iteration when  $B_z$  consists of a small number of straight segments, and, in particular, can promptly improve a poor choice for the initial sequence  $\{\Delta u_k^{(0)}\}$ .

## 4. Boundary composed of straight segments

### 4.1. Numerical integration

If  $B_z$  is composed of straight segments only, the generalized SCE reduces to

$$\frac{dz}{dw} = e^c \prod_i [\sin \frac{1}{2}(w - u_i)]^{\alpha_i}. \quad (4.1)$$

The iteration procedures described in Section 3 require that (4.1) be integrated accurately. If  $B_z$  has a corner at  $u_k$  with an interior angle  $\phi_k$ , the right-hand side of (4.1) has a singularity of the type  $(w - u_k)^{\alpha_k}$ ,  $\alpha_k = -1 + \phi_k/\pi$ . The nonanalytic character of the integrand can lead to errors larger than anticipated even when  $\alpha_k > 0$ . Modified Newton–Cotes rules developed in [4] are very effective in reducing this error.

Let  $u_k$  denote location of a singular corner. Then, (4.1) can be rewritten as

$$z = \int_{w_0}^w f(w)(w - u_k)^\alpha dw + z_0, \quad (4.2a)$$

where

$$f(w) = e^c \left\{ \frac{\sin \frac{1}{2}(w - u_k)}{w - u_k} \right\}^{\alpha_k} \prod_{i \neq k} [\sin \frac{1}{2}(w - u_i)]^{\alpha_i} \quad (4.2b)$$

is nonsingular at  $u_k$  and  $z_0$  corresponds to  $w_0$ . For the purposes of numerical integration,  $f(w)$  is replaced by an interpolating polynomial of the form

$$P_n(w) = C_0 + C_1(w - u_k) + C_2(w - u_k)^2 + \cdots + C_n(w - u_n)^n, \quad (4.3)$$

and the integral in (4.2a) is evaluated analytically. Explicit expressions for the constants  $C_0, \dots, C_n$  for the lower-order rules ( $n = 0$ : modified midpoint rule;  $n = 1$ : modified trapezoidal rule;  $n = 2$ : modified Simpson rule;  $n = 3$ : modified four-point rule) are given in [4]. With  $\Delta$  representing the integration interval, so that  $2\pi/\Delta$  is the number of intervals, and  $\Delta \rightarrow 0$  for increasing accuracy, the leading-order error terms are  $\max(O(\Delta^2), O(\Delta^{2+\alpha}))$  for  $n = 0$ ,  $\max(O(\Delta^2), O(\Delta^2 \log(\Delta^{-1})))$  for  $n = 1$ ,  $\max(O(\Delta^4), O(\Delta^{4+\alpha}))$  for  $n = 2$ , and  $\max(O(\Delta^4), O(\Delta^4 \log(\Delta^{-1})))$  for  $n = 3$  [4]. When  $f(w)$  is even about the singular point, the leading order error term decreases to  $\Delta^2$  for  $n = 0$  and  $\Delta^4$  for  $n = 2$ . The above results suggest that the even rules are not in general “more efficient” than the odd rules, especially when  $\alpha$  is close to  $-1$ .

Integration rule (4.2) has to be explicitly adapted for the neighbourhood of each corner, which is a disadvantage with respect to computer programming. A composite integration rule making allowance for all corners simultaneously may be constructed in the case of the modified midpoint rule [1,4]. Equation (4.1) is rewritten as

$$z = \int_{w_0}^w F(w) \prod_i (w - u_i)^{\alpha_i} dw + z_0, \quad (4.4a)$$

where

$$F(w) = e^c \prod_i \left\{ \frac{\sin \frac{1}{2}(w - u_i)}{w - u_i} \right\}^{\alpha_i} \quad (4.4b)$$

is always nonsingular. Integration on a particular subinterval  $(w_j, w_{j+1})$  is carried out by replacing  $F(w)$  with its midpoint value  $F(\bar{w})$  and evaluating the average value of the remaining product as

$$\prod_i \frac{1}{\Delta} \int_{w_j}^{w_{j+1}} (w - u_i)^{\alpha_i} dw, \quad (4.4c)$$

where the integrations shown are to be carried out analytically. This procedure results in a single general form for an approximate representation of the integral over a subinterval, regardless of the subinterval's location relative to the singularities. The leading order error term is of the same order as in the case of a simple modified midpoint rule [4]. When a corner is placed at  $u = \pi$ ,  $[\sin \frac{1}{2}(w - \pi)]^\alpha$  is singular at both  $u = \pi$  and  $u = -\pi$  due to periodicity and the regularization (4.4b) has to be changed accordingly.

#### 4.2. The saw-tooth boundary

Consider a “saw-tooth” wall, whose fundamental period has two sides, with corners at  $z_0 = (-\pi, 0)$ ,  $z_1 = (x_1, y_1)$ ,  $z_2 = (\pi, 0)$ . Let  $u_0 = -\pi$ ,  $u_1$ ,  $u_2 = \pi$  be the  $u$ -nodes of the

conformal map. In terms of  $\theta_1$ ,  $\theta_2$ , the directions of the sides (with  $\theta(\pi) = \theta_1$ , by the convention of Section 2.3), the turn parameters are  $\alpha = (\theta_2 - \theta_1)/\pi$  at  $z_2$  and  $-\alpha$  at  $z_1$ . From the sum rule (2.14b),

$$u_1 = \frac{\pi(\theta_2 + \theta_1)}{\theta_2 - \theta_1},$$

and the SCE becomes

$$\frac{dz}{dw} = e^{i\theta_1} \left[ \frac{\sin \frac{1}{2}(w - \pi)}{\sin \frac{1}{2}(w - u_1)} \right]^\alpha. \quad (4.5)$$

For the saw-tooth with equal sides,  $\theta_1 = -\theta_2 = -\frac{1}{2}\pi\alpha$  and

$$\frac{dz}{dw} = e^{i\alpha\pi/2} \operatorname{ctg}^\alpha \left( \frac{1}{2}\pi w \right). \quad (4.6)$$

The accuracy and convergence rates of our numerical mapping techniques for straight-segment boundaries can be conveniently tested for regions bounded by saw-tooth profiles because the  $u$ -nodes are known exactly in terms of the initial data.

The lengths of the sides are given, by the rule of sines, as

$$s_1 = \frac{2\pi \sin \theta_2}{\sin(\theta_2 - \theta_1)}, \quad s_2 = \frac{2\pi \sin \theta_1}{\sin(\theta_1 - \theta_2)}.$$

By applying the conformal map rules to this case, we may infer some curious formulas for definite integrals which are not in the standard tables. For example, by setting

$$s_1 = \int_{-\pi}^{u_1} \left| \frac{dz}{dw} \right| du,$$

we get, after some translation and scaling for simplifications,

$$\int_a^b \left\{ \frac{\sin(b-t)}{\sin(t-a)} \right\}^\alpha dt = \frac{\pi \sin[\alpha(b-a)]}{\sin(\pi\alpha)},$$

subject to the limits  $|\alpha| < 1$ ,  $|b-a| \leq \pi$ .

#### 4.3. Numerical examples

The metric coefficient of the mapping  $h = |dz/dw|$  has been selected as a test quantity to verify the accuracy of the numerical solution. Because both the real and imaginary parts of the error  $|dz/dw - dz_c/dw_c|$  are harmonic, its extreme values occur at the boundaries and this is where they are analyzed. Here, the subscript c denotes the computed quantity.

The first test was carried out for the case of a saw-tooth wall with  $\theta_1 = -\frac{1}{4}\pi$ ,  $\theta_2 = \frac{3}{20}\pi$ . Then  $\alpha = 0.4$ ,  $u_1 = -\frac{1}{4}\pi$ ,  $x_1 = -0.3249197\pi$  and  $y_1 = -0.6750803\pi$ . For the phase in (4.5), we have  $\exp(i\theta_1) = (1-i)/\sqrt{2}$ . Numerical results obtained with the modified midpoint rule and displayed in Fig. 2 show that the relative error  $\epsilon = (|dz/dw| - |dz_c/dw_c|)/|dz/dw|$  is consistent with the error of quadrature, i.e.,  $\epsilon = O(|\Delta w|^{1.6})$ .

The second test treated a symmetric saw-tooth wall (equal sides) with turning angle  $-\alpha$  at  $u=0$  and  $+\alpha$  at  $u=\pi$ . The map is given by (4.6). Numerical testing with  $\alpha = 0.5$  shows that

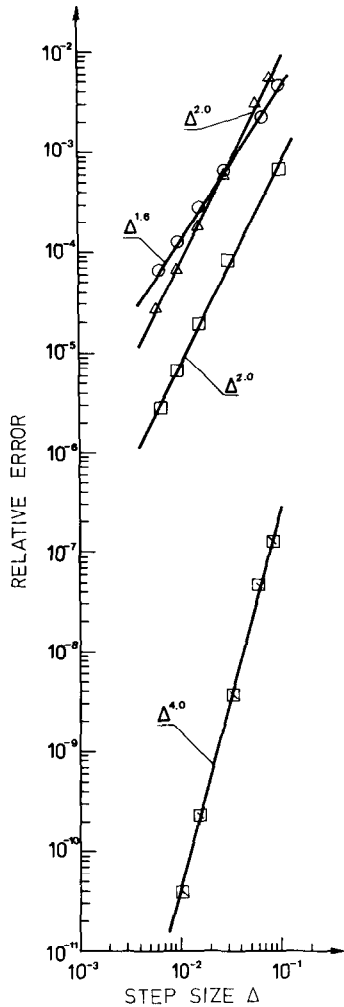


Fig. 2. Accuracy testing of the numerical mapping of a wall composed of straight segments. Top three curves obtained with the modified midpoint integration rule, the bottom one obtained with the modified four-point rule.  $2\pi/\Delta$  defines the number of integration subintervals.  $\circ$  = saw-tooth wall (4.5) with  $\theta_1 = -\frac{1}{4}\pi$ ,  $\theta_2 = \frac{3}{20}\pi$ ,  $\alpha = 0.4$ ;  $\square$  = symmetric saw-tooth wall (4.6) with  $\alpha = 0.5$ ;  $\triangle$  = symmetric saw-tooth wall with  $\alpha = 0.99$ ;  $\blacksquare$  = symmetric saw-tooth wall with  $\alpha = 0.5$ .

the midpoint rule produced higher accuracy,  $\epsilon = O(|\Delta w|^{2.0})$ , due to the fact that the configuration is even around the singularity. The same configuration with  $\alpha = 0.99$  was used to analyze the magnitude of error associated with the mapping of extremely deformed configurations. Results show the error to be still  $\epsilon = O(|\Delta w|^{2.0})$ , while the tenfold deterioration of its absolute value (Fig. 2) occurs due to the fact that the quadrature error is proportional to higher derivatives of the integrand [4]. The increased accuracy of the higher-order rules is demonstrated by applying the four-point rule to the same configuration with  $\alpha = 0.5$ . Figure 2 shows that machine accuracy can be attained with a hundred integration subintervals.

The efficiency of the present solution was compared with the efficiency of the solution described in [2] in the case of a saw-tooth wall with the corners of the fundamental period located at  $z = (0, 0)$ ,  $(0.5, -0.5)$  and  $(1.5, 0.0)$  in the frame of reference used in [2]. The present solution was found to be 6.4 times faster per iteration than the solution of [2] with four terms retained in the infinite product (Section 2.2) and the modified composite midpoint rule used for integration, 9 times faster with six terms, 11.8 times faster with eight terms and 14.6 times faster with ten terms. The number of iterations required for convergence was the same in all cases.

## 5. Boundary geometry and convergence rate of the iteration

### 5.1. Crowding

The severest test of many mapping methods, including this one, is presented by boundaries that cause severe crowding. Typically, these occur in a boundary neighbourhood which lies in a “well”, relative to the rest of the physical region. A mapping method may give good results elsewhere, but virtually no accurate information within the well.

Section 6 explores this condition for certain continuous boundaries. Here, we look at some boundaries made up of straight segments.

Consider the mapping to the upper half  $w$ -plane of the region in the  $z$ -plane above a periodic boundary of straight segments with fundamental period  $0 \leq x \leq 2\pi$ , and nodes at  $z_0 = (0, 0)$ ,  $z_1 = (s_1, 0)$ ,  $z_2 = (s_1, h)$ ,  $z_3 = (2\pi, h)$ ,  $z_4 = (2\pi, 0)$ . This is a periodic step boundary with vertical sides of height  $h$  and well-width  $s_1$ . The nodes on the  $u$ -axis are  $u_0 = 0$ ,  $u_1$ ,  $u_2$ ,  $u_3$ ,  $u_4 = 2\pi$ , with  $u_2 - u_1 = 2\pi - u_3$  by symmetry. The two unknowns of the parameter problem may be taken as the intervals  $\Delta u_1 = u_1 - u_0 = u_1$  and  $\Delta u_2 = u_2 - u_1$ . Then  $\Delta u_4 = u_4 - u_3 = \Delta u_2$  and  $\Delta u_3 = 2\pi - \Delta u_1 - \Delta u_2 - \Delta u_4$ .

Crowding occurs when  $h/s_1 \gg 1$ . As suggested in the Introduction,  $|dz/dw|$  is a useful measure of crowding for a continuously curved boundary, but because corner singularities are handled exactly by SCE methods, we take  $|z_1 - z_0|/|u_1 - u_0| = s_1/\Delta u_1$  as an appropriate analog in the present case. We show, first by a simple estimate, and then by precise calculations, that  $\Delta u_1 \rightarrow 0$  at an exponential rate as a function of increasing  $h/s_1$ .

### 5.2. Crowding estimates for the periodic vertical step

We have

$$\frac{ds}{du} = \frac{|\sin \frac{1}{2}(u - u_2) \sin \frac{1}{2}(u - u_3)|^{1/2}}{|\sin \frac{1}{2}u \sin \frac{1}{2}(u - u_1)|^{1/2}} \quad (5.1)$$

and

$$s_1 = \int_0^{u_1} \frac{ds}{du} du, \quad h = \int_{u_1}^{u_2} \frac{ds}{du} du. \quad (5.2)$$

Assuming that  $u_1$  is very small, we have  $\Delta u_2 \approx u_2$  and  $u_3 \approx 2\pi - u_2$ . Both the above integrals are dominated by the integration region about  $u = u_1$ , where  $ds/du$  is singular, and the

Table 1

 $s_1/(2\pi) = 0.1$ 

$h$	$\Delta u_1$	$\Delta u_2$	$(\Delta u_1)_{\text{est}}$	$(\Delta u_2)_{\text{est}}$	$N_{\text{iter}}$
2.0	$2.67674 \cdot 10^{-5}$	0.200321	$4.5 \cdot 10^{-5}$	0.200358	52
4.0	$1.21524 \cdot 10^{-9}$	0.200335	$2.1 \cdot 10^{-9}$	0.200335	80
6.0	$5.51718 \cdot 10^{-14}$	↓	$9.3 \cdot 10^{-14}$	↓	119
8.0	$2.50480 \cdot 10^{-18}$	↓	$4.2 \cdot 10^{-18}$	↓	160
10.0	$1.13718 \cdot 10^{-22}$	(same)	$1.9 \cdot 10^{-22}$	(same)	203

denominator may be approximated by  $\frac{1}{2}|u(u - u_1)|^{1/2}$ . The numerator contributes mostly near  $u = u_1 \approx 0$ , and can be approximated by  $\sin \frac{1}{2}\Delta u_2$ . Then

$$s_1 \approx 2 \sin \frac{1}{2}\Delta u_2 \int_0^{u_1} \frac{du}{[u(u_1 - u)]^{1/2}} = 2\pi \sin \frac{1}{2}\Delta u_2,$$

$$h \approx 2 \sin \frac{1}{2}\Delta u_2 \int_{u_1}^{u_2} \frac{du}{[u(u - u_1)]^{1/2}} \approx 2 \sin \frac{1}{2}\Delta u_2 \log \left( \frac{4\Delta u_2}{\Delta u_1} \right).$$

The estimates for the first two  $u$ -intervals in the limit of large  $h/s_1$  become

$$(\Delta u_1)_{\text{est}} = 8 \sin^{-1} \left( \frac{s_1}{2\pi} \right) \exp \left( \frac{-\pi h}{s_1} \right), \quad (5.3)$$

$$(\Delta u_2)_{\text{est}} = 2 \sin^{-1} \left( \frac{s_1}{2\pi} \right). \quad (5.4)$$

### 5.3. Representative numerical results

Tables 1 and 2 show computed values of  $\Delta u_1$ ,  $\Delta u_2$  and of  $N_{\text{iter}}$ , the number of iterations of the present method necessary to achieve accuracies of one part in  $10^{10}$ . Also shown are the estimates of the previous subsection which presumed large crowding. Table 1 shows the approach to crowding for fixed well-width  $s_1/(2\pi) = 0.1$  and height  $h$  increasing from 2 to 10. Table 2 shows the approach to crowding for  $h = 10$  and  $s_1/(2\pi)$  decreasing from 0.9 to 0.1.

Because we are testing the effect of boundary geometry on convergence rate, rather than the errors of an integration rule, we choose a rule which is essentially exact for the cases and

Table 2

 $h = 10.0$ 

$s_1/(2\pi)$	$\Delta u_1$	$\Delta u_2$	$(\Delta u_1)_{\text{est}}$	$(\Delta u_2)_{\text{est}}$	$N_{\text{iter}}$
0.9	$2.48782 \cdot 10^{-2}$	2.22711	$3.9 \cdot 10^{-3}$	2.211	42
0.7	$3.59119 \cdot 10^{-3}$	1.54900	$7.9 \cdot 10^{-4}$	1.5512	45
0.5	$1.39796 \cdot 10^{-4}$	1.04713	$4.5 \cdot 10^{-5}$	1.04722	51
0.3	$1.03610 \cdot 10^{-7}$	0.609385	$5.8 \cdot 10^{-8}$	0.609385	64
0.1	$1.13718 \cdot 10^{-22}$	0.200335	$1.9 \cdot 10^{-22}$	0.200335	203

accuracies considered. The sides  $(z_1, z_2)$  and  $(z_3, z_4)$  of the well were divided into ten intervals. Integrals over these intervals and over the vertical segments of the boundary were evaluated by 128-node Gauss–Jacobi quadrature, with endpoint singularities taken into account in the quadrature weight functions. For most of the data in the tables, this was overkill, but this order of precision is required for the extreme case, for which  $s_1/(2\pi) = 0.1$ ,  $h = 10$  and  $\Delta u_1 \approx 10^{-22}$ . Computing time was ten milliseconds per iteration on a CRAY Y-MP.

To compute  $s_1$  from (5.2), one needs differences  $u - u_1$  which, in the extreme case considered, would be less than  $10^{-22}$ . To avoid cancellation error, we chose to set  $u_0 = 0$  and hence  $u_1 \approx 10^{-22}$  rather than, say,  $u_0 = \pi$ ,  $u_1 = \pi + 10^{-22}$ . Suppose, however, the boundary had several centers of crowding, at  $z_a = z(u_a)$ ,  $z_b = z(u_b)$ , etc. To forestall cancellation error, one might employ several  $u$ -variables simultaneously, e.g.,  $u^A = u - u_a$ ,  $u^B = u - u_b$ , etc., and for each  $s_i$ -integral, choose the most appropriate one for integration variable.

The number of iterations required for the chosen accuracy level is seen to vary directly and smoothly with  $\log(1/\Delta u_1)$  and hence with  $h$  and  $s_1$ . In Table 1, the relation is  $N_{\text{iter}} \approx 21h - 7$ . The data may serve as benchmarks for comparison of the present method with other methods.

#### 5.4. Acceleration of iteration

Suppose the acceleration technique of Section 3.4 is applied to the case of a vertical step for which  $s_1/(2\pi) = 0.1$ ,  $h = 10.0$ , which was listed in the tables as requiring 203 iterations for an accuracy of one part in  $10^{10}$ . If (a) the acceleration correction is applied at step  $n$  when the  $\rho_k^{(n)}$  do not vary from a median value by more than 0.5%, and (b) the amount of correction is reduced by a “relaxation factor” of 0.5 (this avoids driving the small magnitude  $u_1$  negative), then the number of iterations required by the same accuracy criterion is 177, an improvement of 15%

As an example where the improvement is somewhat larger, consider a periodic step with sloping sides, with nodes  $z_0 = (0, 0)$ ,  $z_1 = (s_1, 0)$ ,  $z_2 = (s_1 - s_2, h)$ ,  $z_3 = (2\pi - s_2, h)$ ,  $z_4 = (2\pi, 0)$ , and in particular, let  $s_1/(2\pi) = 0.2$ ,  $s_2 = 4.0$ ,  $h = 4.0$ . The small interior angle of  $\frac{1}{4}\pi$  at  $z_1$  intensifies the crowding. We find by calculation that  $\Delta u_1 \sim 7.86791 \cdot 10^{-9}$ ,  $\Delta u_2 = 0.216176$ ,  $\Delta u_3 = 5.41847$  and  $\Delta u_4 = 0.618530$ . Without acceleration, 104 iterations are needed for one in  $10^{10}$  accuracy. For acceleration with the  $\rho$  variation criterion at 1% and a relaxation factor of 0.9, there is improvement in the convergence rate by 26%, to 77 iterations. Larger improvements would accrue at lesser crowding, because then the overall character of iteration convergence is smoother.

### 6. Continuously curved boundary

#### 6.1. Mapping equation

If  $B_z$  is made up of only a single analytic curve, the mapping equation is given by (2.9a). For the purposes of numerical calculations,  $B_z$  is represented by a sequence of boundary points  $z_k$ ,  $0 \leq k \leq N$ , tangents at these points  $\theta_k = \theta(z_k)$  and, perhaps, derivatives of tangents (curvature) at the same points. The type of data that is specified has an effect on the accuracy of

representation of  $B_z$ , and on the accuracy of mapping through the type of approximation that can be constructed for  $\theta(u)$ . The mapping equation takes the form

$$\frac{dz}{dw} = e^c \prod_{j=1}^N \exp \left[ -\frac{I_j(w)}{\pi} \right], \quad (6.1)$$

where  $I_j$  are analytic functions of  $w$  defined by (3.4). The functional form of  $I_j$  depends on the type of approximation constructed for  $\theta(u)$ , as discussed in Section 3.2. One may note that each term in the product in (6.1) represents contribution of one subinterval that is defined in terms of two subsequent points  $(z_{j-1}, z_j)$ .

The mapping is completely determined if a sequence of points  $\{u_k\}$  on  $B_w$  corresponding to the specified set  $\{z_k\}$  defining  $B_z$  has been determined. This can be accomplished by iteration procedures described in Section 3. The required accurate integration of (6.1) does not pose major problems because the integrand is not singular.

Each interval  $(u_{j-1}, u_j)$  defines an integration subinterval for the purposes of numerical integration of (6.1). Midpoint, trapezoidal and Simpson rules have been implemented in the present study. The three- and five-point rules have been used for approximation of  $\theta(u)$  or, equivalently, for evaluation of the inner integral  $I_j(w)$ . Error discussion is given in Section 6.3.

## 6.2. The spike-like boundary

Consider a “spike”-like wall illustrated in Fig. 3, whose mapping onto  $R_w$  is described by

$$e^{-iz} = e^{-iw} \cosh D + \sinh D. \quad (6.2)$$

The height of the spike, i.e., distance between the spike’s top and bottom in the  $z$ -plane, is  $2D$  (Fig. 3). An increase of  $D$  leads to a more deformed configuration and, in the limit  $D \rightarrow \infty$ , the spike assumes rectangular form. The accuracy and convergence rates of our numerical mapping techniques for continuously curved boundaries can be conveniently tested by spike profiles

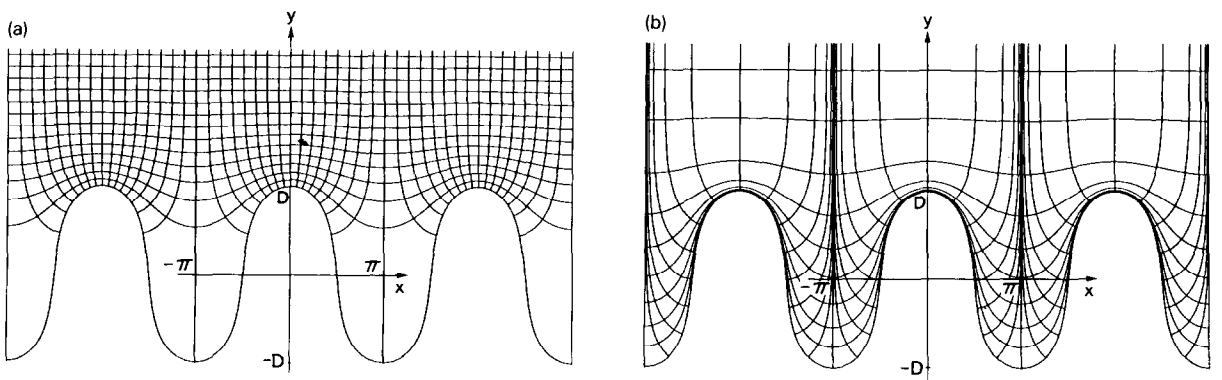


Fig. 3. Spike-like boundary in the  $z$ -plane (6.2) with  $D = 3$ . (a) Grid lines that are equidistant in the  $w$ -plane; (b) grid lines that correspond to constant  $\Delta s$  in the  $z$ -plane.

because the mapping function is known exactly. In addition, since an increase of  $D$  increases the crowding problem, spike profiles provide good tests for determination of the limits of applicability of the numerical method and its ability to deal accurately with highly deformed configurations. The effects of crowding are illustrated by noting that  $|dz/dw|_{\max}$  at the wall is  $\sim 4$  for  $D = 1$ ,  $\sim 110$  for  $D = 3$  and  $\sim 10^4$  for  $D = 5$ .

### 6.3. Numerical examples

Application of the SCE equation requires representation of the boundary curve in terms of a discrete set of points. While locations of these points can be chosen arbitrarily, their selection strongly affects the effective accuracy of the mapping. Here, three approaches, namely, constant- $\Delta u$ , constant- $\Delta x$  and constant- $\Delta s$  distributions, will be used for illustration purposes. The constant- $\Delta u$  approach can be implemented only because in this case the image points on the physical boundary are known in advance from the exact solution (6.2). We include it merely to illustrate the inadequacy of a constant- $\Delta u$  grid in cases of crowding.

In the constant- $\Delta u$  method, the trough of a highly deformed curve is inaccurately represented (Fig. 3(a)) and this suggests using either constant- $\Delta x$  or constant- $\Delta s$  (the most accurate)

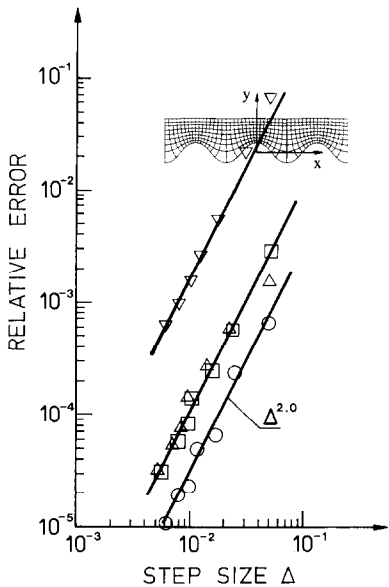


Fig. 4. Accuracy testing of the mapping of a continuously curved wall for the spike profile described by (6.2) with  $D = 1$ .  $\Delta^{-1}$  describes the number of points defining the boundary curve. See text for details.  $\nabla$  and  $\circ$  = test point at  $x/\pi = -0.95$  for constant- $\Delta u$  and constant- $\Delta x$  distributions, respectively;  $\triangle$  and  $\square$  = test point at  $x/\pi = 0$  for constant- $\Delta u$  and constant- $\Delta x$  distributions, respectively.

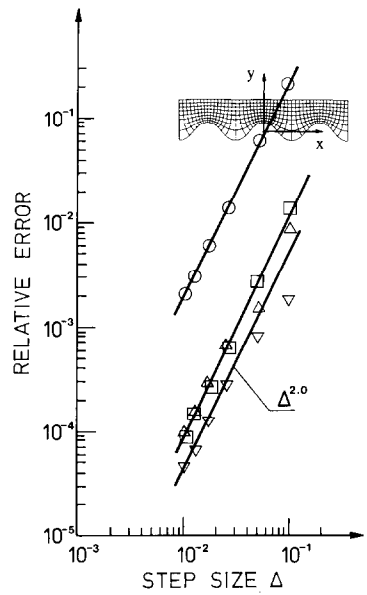


Fig. 5. Accuracy testing as in Fig. 4.  $\circ$  and  $\square$  = test point at  $x/\pi = -1$  for constant- $\Delta u$  and constant- $\Delta s$  distributions, respectively;  $\triangle$  and  $\nabla$  = test point at  $x/\pi = 0$  for constant- $\Delta u$  and constant- $\Delta s$  distributions, respectively.

distributions (Fig. 3(b)). When the mapping is used for grid generation purposes, selection of a uniform grid in the computational ( $w$ -)plane results in the absence of grid points inside the spike (Fig. 3(a)). While the grid corresponding to a constant  $\Delta s$  in the physical ( $z$ -)plane does place a sufficient number of grid points inside the spike, it also creates an unnecessary concentration (crowding) of horizontal grid lines at the top of the spike and vertical grid lines at the edges of the spike (Fig. 3(b)); furthermore, it also leads to a nonuniform grid distribution in the computational ( $w$ -)plane. If good accuracy at the trough of a highly deformed curve is required, a grid corresponding to a constant- $\Delta s$  distribution is unavoidable.

The relative error of the metric coefficient of the mapping has been selected as a test quantity, as in Section 4.3. The magnitude of the error was found to depend continuously on the location along the boundary. Points located around the extremes of the curve, i.e., top and bottom of the spike, have been selected to illustrate the accuracy of the numerical mapping.

In the first test,  $D = 1$  and the boundary is represented by points with constant- $\Delta u$  and constant- $\Delta x$  distributions. Results displayed in Fig. 4 have been obtained with the three-point rule for the inner integral (Sections 3.2 and 3.3) with the phase condition implemented

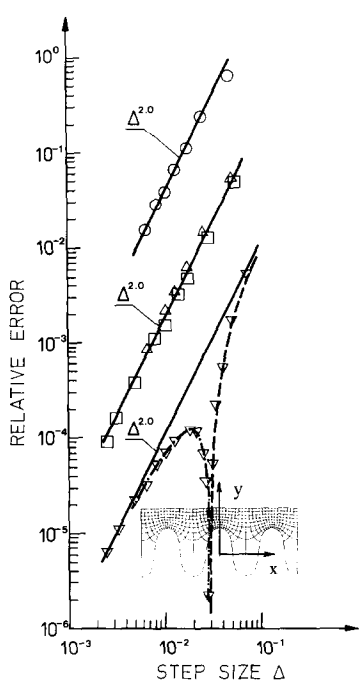


Fig. 6. Accuracy testing as in Fig. 4 with  $D = 3$ .  $\circ$  and  $\square$  = test point at  $x/\pi = -0.95$  for constant- $\Delta x$  and constant- $\Delta s$  distributions respectively;  $\triangle$  and  $\nabla$  = test point at  $x/\pi = 0$  for constant- $\Delta x$  and constant- $\Delta s$  distributions respectively.

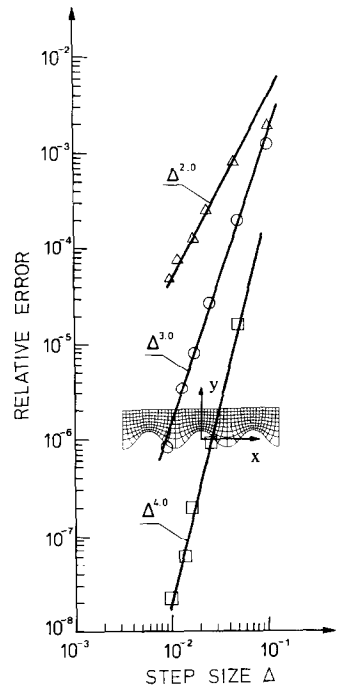


Fig. 7. Accuracy testing as in Fig. 4. All results are for the test point at  $x/\pi = 0$  and constant- $\Delta s$  point distribution.  $\triangle$  = three-point inner integration, composite midpoint rule for the outer integration;  $\circ$  = three-point inner rule, Simpson's outer rule;  $\square$  = five-point inner rule, Simpson's outer rule.

(accuracy  $\sim O(\Delta^3)$ ) and the composite midpoint rule (accuracy  $\sim O(\Delta^2)$ ) for the outer integral (Section 4.1). The resulting total error is dominated by the error of the outer integration, i.e., it is  $\sim O(\Delta^2)$  (Fig. 4). In the case of a constant- $\Delta u$  representation of the boundary, the bottom of the spike is poorly described and this leads to a large local error (Fig. 4). A change to the constant- $\Delta x$  representation results in a redistribution of the points along the arc length and reduction of the error at the bottom of the spike by two orders of magnitude, without increasing the error at the top (Fig. 4). Thus, a considerable error reduction and equilibration of its distribution along the wall can be realized without any additional computational cost by better selection of points defining the boundary.

Figure 5 illustrates the change in the magnitude of the error resulting from implementation of the constant- $\Delta s$  rather than the constant- $\Delta u$  point distribution. The errors in both cases are comparable. The advantages of using constant- $\Delta s$  distributions become obvious for more deformed configurations, such as the one represented by spike (6.2) with  $D = 3$ .

Figure 6 shows that the constant- $\Delta s$  representation of the boundary leads to a reduction of the error by almost two orders of magnitude (as compared to the constant- $\Delta x$  case) without any additional computational effort. It is worth noting here that theoretical analysis gives only an upper bound on the error, i.e., the error may fluctuate between zero and this bound in the actual calculations. Figure 6 illustrates difficulties in experimental verification of error variations as a function of  $\Delta$ . Erroneous conclusions may be reached if an insufficiently wide range of variations of  $\Delta$  (at least two orders of magnitude) is subject to testing. Figure 6 also illustrates capabilities of the method for dealing with highly deformed configurations. One should note a general increase of the level of error for the spike with  $D = 3$  as compared to the spike with  $D = 1$  and a relative loss of accuracy at the bottom of the spike as compared to its top.

The level of error can be reduced by employing higher-order integration rules, as illustrated in Fig. 7. The accuracy  $\sim O(\Delta^3)$  has been obtained by replacing the composite midpoint rule for the outer integral with Simpson's rule, and a further decrease to the level of  $\sim O(\Delta^4)$  resulting from implementation of the five-point rule for the inner integral with the phase condition implemented (Sections 3.2 and 3.3). In the last case an almost machine accuracy is obtained with only 100 points used to define the boundary curve.

## 7. Summary

Schwarz–Christoffel methods for conformal mapping of regions with a periodic boundary have been developed. These methods utilize the generalized Schwarz–Christoffel equation and can deal with boundaries of arbitrary form, i.e., made up of straight and curved segments meeting at corners. Higher-order quadrature rules have been implemented in order to assure highly accurate numerical mapping. The calculated examples show that an accuracy of up to  $\sim O(\Delta^4)$ , where  $\Delta$  is the integration subinterval, can be easily achieved. This accuracy is sufficient for most practical applications. The proposed methodology can be further extended to provide accuracy of  $O(\Delta^5)$ ,  $O(\Delta^6)$ , and higher if necessary. An additional accuracy gain can be realized (without any computational penalty) by a judicious selection of grid points defining the curved segments of the boundary. Methods described here are of particular interest in grid generation for higher-order compact finite-difference discretization schemes.

## Appendix

We compute the integrals  $Q_{jm}(w)$ :

$$Q_{jm}(w) = \int_{u_{j-1}}^{u_j} \log \sin \frac{1}{2}(w - u') \, d(\sin^m \frac{1}{2}(u' - \bar{u}_j)), \quad (\text{A.1})$$

for positive integers  $m$  and  $\bar{u}_j = \frac{1}{2}(u_j + u_{j-1})$ . These are needed for the inner integrations of the SCE. To simplify, set

$$t' = \frac{1}{2}(u' - \bar{u}_j), \quad t = \frac{1}{2}(w - \bar{u}_j), \quad t_0 = \frac{1}{2}(u_j - \bar{u}_j),$$

and integrate by parts:

$$\begin{aligned} Q_{jm}(w) &= \int_{-t_0}^{t_0} \log \sin(t - t') \, d(\sin^m t') \\ &= \sin^m t_0 [\log \sin(t - t_0) - (-1)^m \log \sin(t + t_0)] - B_m, \end{aligned} \quad (\text{A.2})$$

where

$$B_m = - \int_{-t_0}^{t_0} \sin^m t' \frac{\cos(t - t')}{\sin(t - t')} \, dt'. \quad (\text{A.3})$$

Apply

$$\sin t' \cos(t - t') = \sin t - \cos t' \sin(t - t')$$

to (A.3) for  $m \geq 1$  to get

$$B_m = \frac{\sin t_0}{m} (1 - (-1)^m) - \sin t \int_{-t_0}^{t_0} \frac{\sin^{m-1} t'}{\sin(t - t')} \, dt'. \quad (\text{A.4})$$

Apply

$$\sin t' = \cos(t - t') \sin t - \sin(t - t') \cos t$$

to (A.4) for  $m \geq 2$  to get

$$B_m = \frac{\sin t_0}{m} (1 - (-1)^m) + \sin t \cos t \int_{-t_0}^{t_0} \sin^{m-2} t' \, dt' + \sin^2 t B_{m-2}.$$

The  $B_m$  is now reduced to elementary cases for  $m = 1, 2$ , and to recursion relations. We find

$$\begin{aligned} B_1 &= 2 \sin t_0 + \sin t \log \frac{\tan \frac{1}{2}(t - t_0)}{\tan \frac{1}{2}(t + t_0)} \\ &= 2 \sin \frac{1}{4}(u_j - u_{j-1}) + \sin \frac{1}{2}(w - \bar{u}_j) \log \frac{\tan \frac{1}{4}(w - u_j)}{\tan \frac{1}{4}(w - u_{j-1})}, \end{aligned} \quad (\text{A.5a})$$

$$\begin{aligned} B_2 &= t_0 \sin 2t + B_0 \sin^2 t \\ &= \frac{1}{4}(u_j - u_{j-1}) \sin(w - \bar{u}_j) + \sin^2 \frac{1}{2}(w - \bar{u}_j) \log \frac{\sin \frac{1}{2}(w - u_j)}{\sin \frac{1}{2}(w - u_{j-1})}, \end{aligned} \quad (\text{A.5b})$$

$$B_3 = \frac{2}{3} \sin^3 t_0 + B_1 \sin^2 t, \quad (\text{A.5c})$$

$$B_4 = \frac{1}{2} t_0 \sin 2t - \frac{1}{4} \sin 2t \sin 2t_0 + B_2 \sin^2 t, \quad (\text{A.5d})$$

where

$$B_0 = \log \frac{\sin(t - t_0)}{\sin(t + t_0)}.$$

Note that the first term of  $Q_{jm}$  in (A.2) develops a singularity proportional to  $\sin''t \log \sin(t \pm t_0)$  when  $t = \pm t_0$ , that is, when  $w = u_j$  or  $u_{j-1}$ . However, this can be verified to cancel against the same singularity in the  $B_m$  contribution to  $Q_{jm}$ .

## References

- [1] R.T. Davis, Numerical methods for coordinate generation based on the Schwarz–Christoffel transformation, AIAA Paper 79-1463, 4th Comput. Fluid Dynamics Conf., 1979.
- [2] J.M. Floryan, Conformal-mapping-based coordinate generation for flows in periodic configuration, *J. Comput. Phys.* **62** (1986) 221–247.
- [3] J.M. Floryan and C. Zemach, Schwarz–Christoffel transformations — a general approach, *J. Comput. Phys.* **72** (1987) 347–371.
- [4] J.M. Floryan and C. Zemach, Quadrature rules for singular integrals with application to Schwarz–Christoffel mappings, *J. Comput. Phys.* **75** (1988) 15–30.
- [5] M. Hoekstra, Coordinate generation in symmetrical interior, exterior or annular 2-D domains, using a generalized Schwarz–Christoffel transformation, in: J. Häuser and C. Taylor, Eds., *Numerical Grid Generation in Computational Fluid Dynamics*, Proc. Internat. Conf., Landshut (Pineridge, Swansea, 1986) 59–70.
- [6] R. Menikoff and C. Zemach, Methods for numerical numerical conformal mapping, *J. Comput. Phys.* **36** (1980) 366–410.
- [7] R. Menikoff and C. Zemach, Rayleigh–Taylor instability and the use of conformal maps for ideal fluid flow, *J. Comput. Phys.* **51** (1983) 28–64.
- [8] K.P. Sridhar and R.T. Davis, A Schwarz–Christoffel method for generating internal flow grids, in: K.N. Ghia, T.S. Mueller and B.R. Patel, Eds., *Computers in Flow Predictions and Fluid Dynamics Experiments* (ASME (Mech. Engineers), New York, 1981) 35–44.
- [9] J. Stoer and R. Bulirsch, *Introduction to Numerical Analysis* (Springer, New York, 1980).
- [10] C. Zemach, A conformal map formula for difficult cases, in: L.N. Trefethen, Ed., *Numerical Conformal Mapping* (North-Holland, Amsterdam, 1986) 207–215; also: *J. Comput. Appl. Math.* **14** (1 & 2) (1986) 207–215.